

Autonomous Optimization of Fluid Systems at Varying Length Scales

Alexander E. Siemann^{a,1}, Evyatar Shaulsky^b, Matthew Beveridge^c, Tonio Buonassisi^a, Sara M. Hashmi^b, and Iddo Drori^{c,2}

^aDepartment of Mechanical Engineering, Massachusetts Institute of Technology, Cambridge, MA 02139; ^bDepartment of Chemical Engineering, Northeastern University, Boston, MA 02115; ^cDepartment of Electrical Engineering and Computer Science, Massachusetts Institute of Technology, Cambridge, MA 02139

Autonomous optimization is a process by which hardware conditions are discovered that generate an optimized experimental product without the guidance of a domain expert. We design an autonomous optimization framework to discover the experimental conditions within fluid systems that generate discrete and uniform droplet patterns. Generating discrete and uniform droplets requires high-precision control over the experimental conditions of a fluid system. Fluid stream instabilities, such as Rayleigh-Plateau instability and capillary instability, drive the separation of a flow into individual droplets. However, because this phenomenon leverages an instability, by nature the hardware must be precisely tuned to achieve uniform, repeatable droplets. Typically this requires a domain expert in the loop and constant re-tuning depending on the hardware configuration and liquid precursor selection. Herein, we propose a computer vision-driven Bayesian optimization framework to discover the precise hardware conditions that generate uniform, reproducible droplets with the desired features, leveraging flow instability without a domain expert in the loop. This framework is validated on two fluid systems, at the micrometer and millimeter length scales, using microfluidic and inkjet systems, respectively, indicating the application breadth of this approach.

1. Introduction

Generating discrete and uniform droplets from a fluid stream requires the fine-tuning of experimental conditions to transition the flow from a continuous, stable jet to a separated, unstable stream of droplets (1). We explore this transition through two distinct driving forces: gravity-driven fluid flow through air, and pressure-driven flow of two immiscible fluids. Rayleigh-Plateau instability governs the separation of a fluid stream into discrete droplets through gravity-driven perturbations and capillary instability governs the separation of a fluid stream into discrete droplets through pressure-driven perturbation (2). These fluid stream instabilities are controllable by varying the applied forces and experimental conditions of the fluid systems (1, 3). However, the exact combination of conditions that produce discrete droplets is often analytically expensive

All authors designed research, wrote the paper, and contributed to scientific discussions and manuscript review; A.E.S. and E.S. collected data; A.E.S., M.B., I.D., and T.B. developed machine learning models; A.E.S and E.S. developed software; A.E.S. and T.B. developed hardware; A.E.S., S.M.H., and E.S. analyzed data.

Two of the co-authors (A.E.S., T.B.) are also co-authors on IP describing one of the deposition system. One of the authors (T.B.) owns equity in a start-up company applying machine learning to materials.

¹To whom correspondence should be addressed. E-mail: asiemenn@mit.edu

²To whom correspondence should be addressed. E-mail: idrori@mit.edu

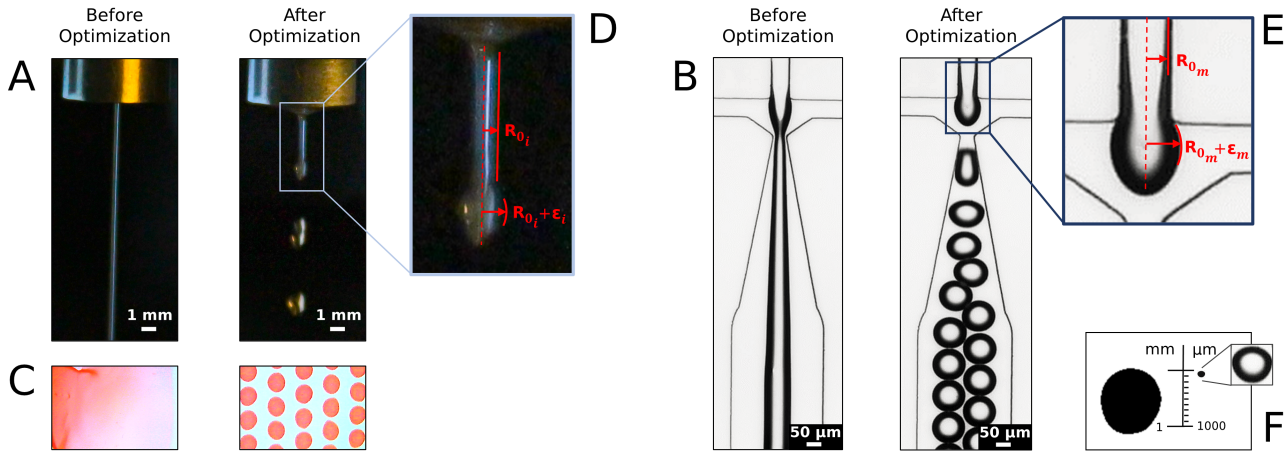


Fig. 1. Controlling fluid stream instability through autonomous Bayesian optimization. (A) An instance of the Rayleigh instability phenomenon within inkjet-generated droplets and (B) an instance of the capillary instability phenomenon within microfluidic-generation droplets after using Bayesian experimentation to optimize experimental conditions to maximize droplet yield and uniformity. Before optimization, the Latin Hypercube sampling-initialized samples used experimental conditions which performed poorly. Without the injection of knowledge from a domain expert, Bayesian experimentation-in-loop autonomously discovered conditions which control the instabilities of the fluid jet. (C) An instance of inkjet-generated droplet structures deposited onto a platen before and after Bayesian optimization of conditions. Bayesian experimentation controls the fluid system conditions that produce (D) Rayleigh instabilities within the inkjet-generated jet of radius R_{0i} by applying piezoelectric-driven perturbations of size ε_i and (E) capillary instabilities within the microfluidics-generated jet of radius R_{0m} by applying viscous stress-driven perturbations of size ε_m . (F) Length scale comparison of an inkjet-generated droplet (left in mm) and a microfluidic-generated droplet (right in μm).

to compute due to the complex, nonlinear physical relationships between all forces acting on the fluid (4). Moreover, the discovery of droplet-generating conditions via experimentation requires resource-intensive trial-and-error experimentation or guidance of a human domain expert. Therefore, analytical models and domain experts are replaced by Bayesian machine learning methods to efficiently discover the experimental conditions where Rayleigh and capillary instabilities exist and generate optimized droplets (5–7).

We have all playfully tested the perfect setting that makes running water turn into drops, by opening or closing a faucet by just the right amount. In this work, we explore the question: can we use machine learning and computer vision to identify the optimal droplet formation conditions in different hardware, without a domain expert or prior analytical model in the loop? We demonstrate this is feasible for a range of fluid systems with multiple parameters across different scales, and develop a computer vision-driven Bayesian optimization (BO) framework to automate the discovery of a narrow window of unstable experimental conditions that produce optimized droplet structures without a domain expert or analytical model.

The robustness of this framework is demonstrated via application to two fluid systems of distinct length scales: (1) an inkjet system that generates droplets at the millimeter length scale through piezoelectric and gravity-induced Rayleigh instability and (2) a microfluidic system that generates droplets the micrometer length scale through viscous stress and pressure-induced capillary instability, both shown in Fig. 1.

Optimized droplet structures are generated by a fluid system with fine-tuned conditions that promote fluid instability within a jetting regime (8, 9). In this paper, droplets are generated in the inkjet fluid system by tuning three conditions: fluid pressure, piezoelectric actuation frequency, and nozzle translation speed; droplets are generated in the microfluidic system by tuning two conditions: water pressure and oil pressure. Optimized droplet structures are defined as having: (1) maximum geometric uniformity and (2) maximum yield (*i.e.*, high count of large droplets). Generating uniform, high yield droplets has importance across several application fields conditional on the length scale such as (1) at the millimeter length scale to create droplets used for high-throughput characterization of semiconductor properties and (2) at the micrometer length scale to create droplets used for the efficient delivery of controlled volumes of material for biomedical or cosmetic applications. However, within a jetting regime where droplets are under high-velocity conditions, droplet formation phenomena depend in a nonlinear way on velocity, pressure, interfacial tension, and viscosity (10). The difficulty of solving the nonlinear dynamics drives the significance of this paper to develop a framework that outputs tuned experimental condition values for generating optimized droplets without having to program or analytically model these nonlinear dynamics.

A. Main Findings. We demonstrate accurate and repeatable discovery of Rayleigh and capillary unstable regions within two fluid systems at different length scales using autonomous optimization. For each of these fluid systems, three trials of Bayesian optimization were run using three different decision policy acquisition functions in which all trials converged to learning similar bounds for generating uniform and high-yield droplet structures within those bounds. The developed Bayesian optimization and computer vision process loop at-

tains consistent convergence on these learned configuration space topologies using only 60 experimental samples for each acquisition function instance.

2. Methods

To autonomously discover the instability conditions of fluid jets at the millimeter and micrometer length scales, the following process flow is utilized, shown in Fig. 2: (A) configuration space initialization via Latin Hypercube sampling (LHS); (B) inkjet and microfluidic droplet generation using the initialized conditions; (C) characterization of droplet yield and structures via computer vision; (D) Bayesian optimization using fast surrogate acquisition function for predicting the next condition values. After prediction, we evaluate the conditions via experimentation to update the posterior and repeat; (E) iterative convergence on experimental conditions that generate user-defined optimum droplet yield and structure. Processes (B)–(D) comprise the autonomous feedback loop to control the instability of our fluid stream.

A. Configuration Space Dynamics.

A.1. Inkjet System Dynamics. The configuration space of the inkjet fluid system is defined as having three controllable experimental conditions: (1) fluid pressure, (2) piezoelectric actuation frequency, and (3) nozzle translation speed. The space is not constrained by a domain expert which means that BO is given the full gamut of condition permutations to explore and discover an optimum set of conditions. These three conditions all have an influence on the shape and yield of droplets deposited on a plate. Pressurizing the fluid within the pipes drives both the radius and the flow rate of the stream for a fixed orifice size; our inkjet system operates at pressures limits of 0.03–0.15MPa. Applying an alternating current electrical signal to the piezoelectric material within the pipe actuates a membrane at a given frequency to induce perturbations, ε , within the fluid stream; our inkjet system operates at frequency limits of 1.0–600.0Hz. The fluid is ejected from a nozzle which translates above a deposition site, driving the point of deposition of the fluid; our inkjet system operates at translation speed limits of 10–360mm/s. In addition to these three controllable conditions, the printable fluid parameter space is governed by fluid properties such as density, surface tension, and viscosity, along with the driving pressure force and the nozzle geometry (11–13). In this manuscript, we used the same fluid and small nozzle tip radius for all experiments, the fluid being dyed water. The intrinsic fluid properties are constant and we operate at very high flow velocity for all operating pressures.

The complex interplay of all these conditions results in analytically intractable predictions of droplet size and spacing from an inkjet system, therefore illustrating the purpose of using a data-driven BO approach to explore the configuration space.

A.2. Utility of Inkjet Generated Droplets. Depositing these inkjet droplets onto a substrate is a process useful for high-throughput characterization of material, most notably for finding optimized semiconductor materials that maximize efficiency or stability (14, 15). Semiconductors such as perovskites have vast and complex composition spaces which

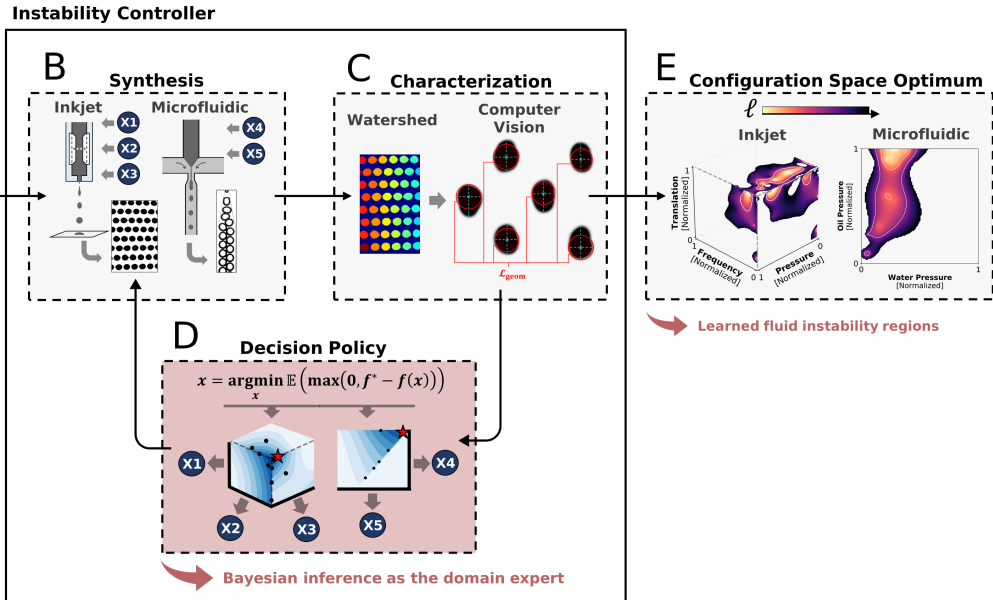


Fig. 2. Process flow for autonomous optimization of discrete and uniform droplet structures. (A) To initialize our Bayesian-guided experiment, LHS is used to sample 20 experimental conditions from the 3-dimensional inkjet configuration space and the 2-dimensional microfluidics configuration space. (B) A human technician plugs the in the 20 LHS-initialized experimental conditions to the inkjet and microfluidic systems, the initial training droplet dataset is generated for BO. (C) Before running the BO of configuration space, each sample in the dataset is assigned a label indicative of droplet yield and structure using computer vision and image processing. A loss function is developed to score droplets within a sample to meet the objective of maximizing yield and structural uniformity; if the sample closely matches this objective, the loss score is low. A human technician is present to take an image of the synthesized sample such that it can be characterized via computer vision. (D) The acquisition decision policy of BO is applied to the inkjet and microfluidics configuration spaces to drive droplet generation towards optimizing the defined objective function. Three decision policy acquisition functions are studied in this paper: expected improvement (EI), maximum probability of improvement (MPI), and lower confidence bound (LCB). The acquisition function outputs 10 new optimized conditions which are then plugged back into the hardware systems to produce new samples that will be used to retrain BO. The iterative retraining of BO from processes (B)–(C) autonomously drives the control of the instability phenomenon without the intervention of a domain expert, as shown in Fig. 1, only using a technician to input the LHS and BO-sampled conditions to the hardware and take an image of the droplets. (E) After four rounds of iteratively retraining BO with new experimentally generated and labeled droplet data, the exploration of inkjet and microfluidic configuration spaces converges to an optimum experimental condition, *i.e.*, using only 60 training samples after four rounds. These conditions are fine-tuned by BO to control the fluid jet instability such that droplets of high yield and uniform structure are consistently generated.

makes it challenging to discover optimum compositions (16–18). Thus, using discrete inkjet-deposited droplets of varying semiconductor compositions for high-throughput experimental characterization elicits an accelerated search of this vast composition space for an optimum composition. However, studies such as *Bash et al.*, (2020) rely on a domain expert to fine-tune experimental conditions that establish Rayleigh instability control of their fluid streams prior to semiconductor characterization. The nonlinear relationships between fluid forces make droplet yield and structure analytically expensive to compute from the experimental hardware condition inputs alone. In this study, we use Bayesian optimization to tune the inkjet hardware conditions of jet pressure, piezoelectric actuation, and nozzle lateral translation speed using a small subset of experimental data rather than analytical equations such that we produce a matrix of optimized discrete droplets.

A.3. Microfluidic System Dynamics. The configuration space of the microfluidic system is defined as having two controllable experimental conditions: (1) the driving pressure of the inner (water) and (2) the outer (oil) fluid phases. The space is unconstrained by a domain expert, hence, BO is given the full gamut of condition permutations to search for an optimum set of conditions. Our study uses a flow-focusing microfluidic device to achieve control over the different flow conditions by varying two immiscible liquid pressures within an operable range of 1.0e-4–0.19MPa (19). Previous studies show three

different droplet formation phases in flow-focusing microfluidic devices: squeezing, dripping, and jetting (20, 21), where droplet size, shape, and generation frequency for a given pressure depend on both the device geometry and fluid properties (10). Droplet properties are primarily governed by two dimensionless numbers: (1) Capillary number (Ca) and (2) Weber number (10, 22, 23):

$$Ca = \frac{\eta \dot{\gamma} a}{\sigma}, \quad [1]$$

$$We = \frac{\rho v^2 a}{\sigma}, \quad [2]$$

where η is the fluid dynamic viscosity, $\dot{\gamma}$ is the shear rate, a is the droplet size, σ is the surface tension, ρ is the fluid density, and v is the flow velocity.

However, a prediction of droplet shape and size as a result of the intrinsic parameters of the system using fluid dynamic simulations for the entire parameter space is still intractable to compute (9). Fig. S5 illustrates the nonlinear relationship between We, Ca, and the objective value, further demonstrating the significance of exploring the experimental configuration space via BO.

A.4. Utility of Microfluidic Generated Droplets. The ability to rapidly create microspheres with a high surface area to volume ratio is beneficial for a large variety of applications such as materials generation, bio(chemical) analysis, polymeric microcap-

sules, and more (24–26). Industries like food science, biomedical, and cosmetics used microcapsules as materials delivery vehicles with the ability to tuning the capsule wall chemistry for slow or triggered release of the encapsulated material (27–29). For each of these unique applications, a different desirable microdroplet volume is required. This droplet volume results from several parameters like the interfacial tension between the immiscible fluids, their viscosities, then microfluidic device geometry, and fluid flow rates (19, 30). While the dependence of drop size and number on a single flow rate in a defined device geometry can be predicted to a certain extent by modeling, the larger parameter space of both flow rates may be cumbersome to explore manually in the laboratory. When changing both device geometry and fluid properties, the experimental lab work is vast. Machine learning processes like BO have the promise to greatly improve the efficiency of exploring parameter space and save expensive lab time resources (5, 31). In this study, we use BO to tune pressures of water and oil into a flow-focusing microfluidic droplet generator to maximize the yield of water drops in a continuous oil phase.

B. Configuration Space Initialization. Without *a priori* knowledge of our configuration space from a domain expert, we look towards using machine learning methods to learn the topology of the nonlinear configuration space dynamics for us. We use BO-in-loop to learn the topology of the configuration space. BO iteratively outputs new optimized conditions to sample within the configuration space using knowledge learned from previous iterations of searching.

To give BO the best chance at finding a global optimum condition, we provide the algorithm with our best estimation of the configuration space as a whole in the form of an initialization dataset. Latin Hypercube sampling (LHS) is a sampling tool that generates an initialization sample set $\mathcal{X}^{(N)}$ that captures the variability of an N -dimensional configuration space with low bias. LHS stratifies the range of each control parameter in S (noted in Section A) into K strata ($K = 20$ in this paper) of equal marginal probability such that each stratum is randomly sampled once to generate $\mathcal{X}^{(N)}$. The low variance demonstrated by LHS relative to random and stratified sampling illustrates the goodness of LHS as an unbiased estimator for selecting initialization conditions (32).

C. Computer Vision Characterization. To determine the instability regions within the configuration space where droplets are optimized for uniformity and yield, each generated sample is labeled. An optimization objective label ℓ is computed for each droplet sample via computer vision which quantifies the uniformity and yield of the droplets. We implement a scalarized linear combination of loss functions to compute the optimization objective of droplet uniformity and droplet yield.

After generating each sample, the droplet structure is optically imaged by a technician and then fed into a watershed segmentation algorithm. The watershed algorithm segments each droplet in the sample from the background, as shown in Fig. 2(C), such that we generate a set of indexed droplet pixels P_{droplet} . We characterize all indexed droplets within a sample by an optimization objective label, $\ell \in [0, 1]$, which we aim to minimize. Droplet uniformity is the first component of ℓ and it is calculated by taking the normalized complement of the intersection between P_{droplet} and a circle mapped perfectly to each uniquely indexed droplet P_{circle} :

$$\mathcal{L}_{\text{geom}} = \frac{\sum P_{\text{drop}} \cap P_{\text{circle}}}{\sum P_{\text{droplet}}}. \quad [3]$$

By computing the major axis chord r_{major} and minor axis chord r_{minor} of each indexed droplet, a perfect circle is mapped to each droplet such that the circle's centroid is the intersection point of r_{major} and r_{minor} and the radius is the $\frac{r_{\text{major}}+r_{\text{minor}}}{2}$. Fig. 2(C) illustrates the process of mapping a circle to each watershed indexed droplet in the sample. We aim to minimize $\mathcal{L}_{\text{geom}} \in [0, 1]$ to achieve droplets of high uniformity.

Droplet yield is the second component of the optimization objective and it is calculated by taking a linear combination of the normalized ratio of non-droplet pixels to all pixels and the normalized droplet count:

$$\mathcal{L}_{\text{yield}} = \frac{1}{2} \frac{\sum \overline{P_{\text{drop}}}}{\sum P_{\text{drop}} \cup P_{\text{drop}}} + \frac{1}{2} \frac{\text{count}(P_{\text{drop}}) - \alpha}{\alpha}, \quad [4]$$

where α is a number sufficiently larger than the possible count of droplets. We implement α to keep ℓ as a minimization problem. We aim to minimize $\mathcal{L}_{\text{yield}} \in [0, 1]$ to achieve droplets of high area and high count.

Thus, the scalarized linear combination of geometric uniformity (Equation 3) and yield (Equation 4) constructs the full optimization objective:

$$\ell = \frac{w_{\text{geom}} \mathcal{L}_{\text{geom}} + w_{\text{yield}} \mathcal{L}_{\text{yield}}}{w_{\text{geom}} + w_{\text{yield}}}, \quad [5]$$

where w_{geom} and w_{yield} are tunable weights for the uniformity and yield components, respectively. In this paper we set $w_{\text{geom}} = w_{\text{yield}}$ such that both geometric uniformity and yield objectives are represented equally during optimization. Every experimentally generated sample is labeled with a value of ℓ such that we aim to minimize $\ell \in [0, 1]$ to achieve droplets of both high geometric uniformity and high yield.

While additional properties like droplet size are not explicitly included in the objective function as described above and used in the present study, the user-defined objective function can be tailored to specific applications as needed.

D. Bayesian Optimization. We drive the efficient discovery of unstable fluid conditions using Bayesian optimization-in-loop. The computer vision-labeled initialization set of samples, $\mathcal{X}^{(N)}$, serve as a likelihood to a surrogate model which uses a decision policy called an acquisition function to move sampling towards regions within the configuration space of low ℓ value, thus, maximizing droplet uniformity and yield. This optimization process is called Bayesian optimization (BO) which is described as (7, 33):

$$x^* = \arg \min_{x \in \mathcal{X}} \ell(x), \quad [6]$$

where x is some vector of printing condition in $\mathcal{X}^{(N)}$.

The surrogate model used to facilitate BO is Gaussian process (GP):

$$\ell(x) \sim \mathcal{GP}(\mu(x), k(x, x')). \quad [7]$$

A Gaussian prior, \mathcal{N} , is assigned to the initial GP likelihood of the objective function $\ell(x)$ that is a function of x , a vector of experimental conditions in the set $\mathcal{X}^{(N)}$, to estimate its posterior mean $\mu(x)$ and (co)variance $k(x, x')$ (7):

$$\mu(x) = \mathbb{E}[\ell(x)], \quad [8]$$

$$k(x, x') = \mathbb{E}[(\ell(x) - \mu(x))(\ell(x') - \mu(x'))]. \quad [9]$$

In this work, three common acquisition functions: (1) expected improvement (EI), (2) maximum probability of improvement (MPI), and (3) lower confidence bound (LCB) are used to guide the iterative selection of x (7, 33). We introduce these three distinct acquisition functions to illustrate the reproducibility of the computer vision-Bayesian optimization-in-loop experimental method for discovering similar regions of unstable fluid conditions in both millimeter and micrometer length scale fluid systems. We begin an experiment by initializing a model with data points. Next, we iterate interleaving sampling and update steps. For every iteration of the BO-in-loop, 10 new optima are output by the GP surrogate acquisition function and are concatenated to $\mathcal{X}^{(N)}$. The decision policies for each acquisition function are described next.

D.1. Expected Improvement Acquisition. Expected improvement (EI) is a decision policy that samples optima x from the GP by evaluating the function $f(x)$ and comparing the value to the current running minimum function evaluation $\ell^* = \min(\ell(x))$. Since our batch size is 10 samples per iteration, the EI acquisition function outputs 10 samples that have the highest improvement from previous ℓ^* (6, 33):

$$a_{\text{EI}}(x) = \int_{-\infty}^{\ell^*} (\ell^* - \ell(x)) \mathcal{N}(\ell; \mu(x), k(x, x')) d\ell. \quad [10]$$

A local penalization evaluator is used which penalizes points closely sampled to each other within a batch, thus, the best point is selected first, then the second best (within some distance), and so on.

D.2. Maximum Probability of Improvement Acquisition. Maximum probability of improvement (MPI) is a decision policy that samples optima x similarly to EI, however, does not scale the function values proportional to the magnitude of improvement. This means that MPI computes the location where $\ell^* = \min(\ell(x))$ but does consider how much the function value ℓ improves from the current running minimum ℓ^* . Thus, the acquisition of MPI is the same as EI but without the $(\ell^* - \ell(x))$

term (6, 33):

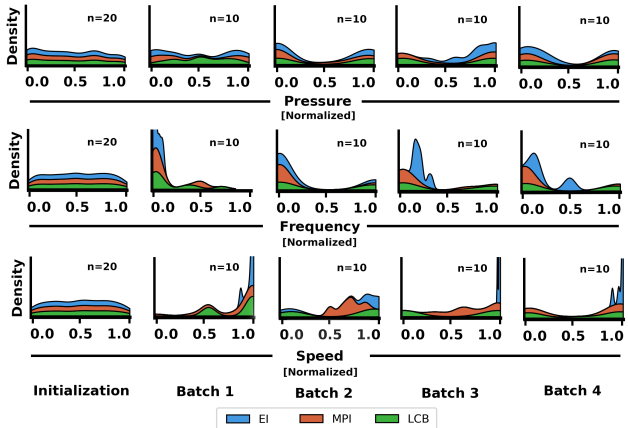
$$a_{\text{MPI}}(x) = \int_{-\infty}^{\ell^*} \mathcal{N}(\ell; \mu(x), k(x, x')) d\ell. \quad [11]$$

D.3. Lower Confidence Bound Acquisition. Lower confidence bound (LCB) is a decision policy samples optima x through an explicit trade-off scheme between exploitation and exploration. A pure exploitation acquisition function outputs optima x exactly at evaluated GP function mean values $\mu(x)$ that minimize ℓ , i.e., where the standard deviation $\sqrt{k(x, x')}$ about the mean is zero. A pure exploration acquisition function outputs optima x within some large number of standard deviations about the mean. The LCB acquisition function balances exploiting the GP mean values with exploring the GP variance by varying a parameter $\beta > 0$ (33):

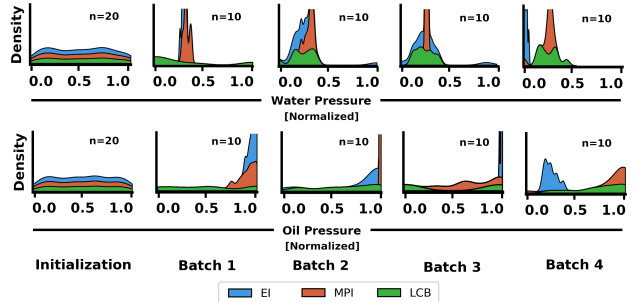
$$a_{\text{LCB}}(x; \beta) = \mu(x) - \beta \sqrt{k(x, x')}. \quad [12]$$

E. Evaluating Convergence Performance. The performance of the three highlighted acquisition functions: (1) EI, (2) MPI, and (3) LCB are compared as batch processes. First, the search mechanics of each acquisition function are analyzed per batch of output optima. We plot the density estimations in Fig. 3 to illustrate the sampling mechanics of each decision policy (Equations 10, 11, and 12) applied to our dataset $\mathcal{X}^{(N)}$ that is labeled with the objective to minimize ℓ , computed using Equation 5. The sampling performance of each acquisition function is then evaluated using the learned configuration space topology that falls within the feasibility bounds.

The learned feasibility bounds demarcate regions within the configuration space where good control over the fluid stream instability is established; regions within the feasibility bounds tend to generate optimal droplet structures while regions outside the feasibility bounds tend to generate failed structures due to a continuous fluid stream flow. The feasible bounds are defined by a threshold optimization objective label of $\ell < 0.75$. This threshold defines the conditions for both the inkjet and microfluidic systems where our fluid stream evolves



(a) Inkjet acquisition function sampling regions density



(b) Microfluidic acquisition function sampling regions density

Fig. 3. Density of printing conditions sampled by each acquisition function over four batches of samples for the (a) inkjet system and (b) microfluidic system. GP-EI, GP-MPI, and GP-LCB are initialized using $n = 20$ LHS printing conditions and then $n = 10$ conditions are sampled iteratively and concatenated to $\mathcal{X}^{(N)}$. The model is updated after each time conditions are sampled and experimentally characterized using ℓ . Roughly each acquisition function for both the inkjet and microfluidic systems converge to a region of each printing condition by batch 4, however, scenarios such as microfluidic GP-EI trade-off sampling convergence in the oil pressure condition for sampling convergence in the water pressure condition between batches 3–4.

from a continuous stream to discrete droplets, as shown by Fig. 4.

In this paper, the sample efficiency of an acquisition function to discover unstable fluid regions is defined as being proportional to the number of low ℓ -valued samples discovered within the feasibility bounds. Fig. 5 quantifies the quality of all the samples output by each acquisition function, using ℓ as a metric for droplet uniformity and yield and as an indirect controller of unstable fluid conditions when $\ell < 0.75$.

3. Results

A. Acquisition Function Sampling. Through computer vision-driven Bayesian experimentation-in-loop, we demonstrate discovery of unstable fluid conditions that generate optimized droplet structures using three different acquisition functions (1) GP-EI, (2) GP-MPI, and (3) GP-LCB applied to two experimental systems of different length scales (1) inkjet and (2) microfluidic. As described in Section 2D, each acquisition function drives a unique sampling of the configuration space to discover optima unstable fluid conditions.

Fig. 3a illustrates the regions of the inkjet configuration space explored by each acquisition function for each batch of BO experimentation. The inkjet system is driven by three controllable parameters of pressure, frequency, and speed that define the configuration space to generate a sample set $X^{(3)}$. For the pressure parameter, all three acquisition functions sample from similar regions clustered at low pressure and high pressure values, creating a bimodal distribution of optima, indicating that at those points the objective is minimized. For the frequency parameter, the sampling of batch 1 begins concentrated at low values of frequency and evolves to begin searching higher values as we iterate. However, by batch 4, EI converges to sampling from non-extrema frequency conditions where new minima are found. For the speed parameter, all three acquisition functions begin sampling from high speed regions until EI converges on searching only high extrema speed conditions while MPI and LCB search both low and high extrema conditions by batch 4.

Fig. 3b illustrates the regions of the microfluidic configuration space explored by each acquisition function. The microfluidic system is driven by two controllable parameters of water pressure and oil pressure that define the configuration space to generate a sample set $X^{(2)}$. For the water pressure parameter, EI and MPI concentrate sampling about low-mid range values for batch 1 and then MPI continues to stay concentrated there. Conversely, by batch 2 EI spreads sampling out to a larger range of low-mid range water pressure values until batch 4 when it concentrates at low extrema water pressure values. LCB begins sampling across the full range of water pressure values for batch 1 and then concentrates at low-mid range values for the rest of the batches. For the oil pressure parameter, both EI and MPI concentrate at high values for batch 1. MPI concentrates at high extrema oil pressure conditions for batch 2 until it begins to re-explore the space in batches 3 and 4. EI concentrates at high extrema oil pressure conditions for batch 3 until it begins exploring low-mid range values for batch 4. LCB stays in an explorative mode for the oil pressure condition for all batches.

The results from Fig. 3 illustrate the unique sampling mechanics of the GP-EI, GP-MPI, and GP-LCB acquisition functions. The learned fluid instability control regions and

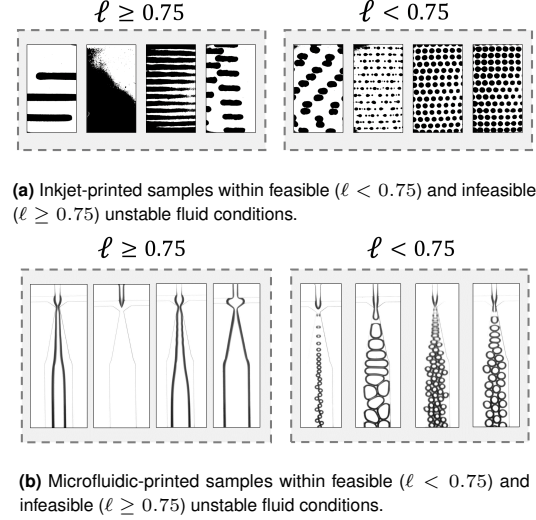


Fig. 4. Experimentally generated droplet samples labeled with the computer vision-computer optimization objective, ℓ for the (a) inkjet system and (b) microfluidic system. Printing conditions that generate a sample with $\ell < 0.75$ are shown to produce discrete droplets, hence, exhibiting the feasibility of Rayleigh and capillary instability occurring at those conditions. Conversely, printing conditions that generate a sample with $\ell \geq 0.75$ are shown to have continuous or connected fluid patterns, implying it is not feasible for Rayleigh or capillary instability to occur at these conditions.

configuration space topology are governed by these sampling mechanics of the BO acquisition functions. It will be shown that for each experiment, the learned configuration spaces are all similar even with each acquisition function having a unique decision policy.

B. Configuration Space Topology. The regions within the configuration space where fluid instability occurs and generates droplets is discovered autonomously through the computer vision-driven BO-in-loop method. Fig. 4 illustrates the sample droplet structures outside of the feasibility bounds ($\ell \geq 0.75$) and inside the feasibility bounds ($\ell < 0.75$). Fig. 5 shows the topology (interpolated ℓ values) of all points sampled within the configuration space for each BO acquisition function. If many of the points sampled by an acquisition function fall within the feasibility bounds, then that acquisition function has a high sample efficiency for discovering the feasibility bounds of unstable fluid conditions of our two fluid systems.

Printing conditions that form discrete droplets due to the presence of instability are classified by having $\ell < 0.75$, while all other printing conditions outside of these bounds generate a continuous fluid stream, leading to failed samples. Fig. 5 demonstrates that each BO acquisition function learns to sample within these bounds without having a domain expert constrain the configuration space *a priori*.

For the inkjet system, the autonomous optimization loop repeatedly discovers the feasible conditions for Rayleigh instability to be in low-mid range frequencies and mid-high range translation speeds using different decision policy acquisition functions. Moreover, Fig. 5a illustrates that this instability may exist for all pressure values within the inkjet system. Within four sequential iterations of acquired sample batches, the following percentages of samples lie within the Rayleigh feasibility bounds for each policy: (1) 65.0% using GP-EI, (2) 45.0% using GP-MPI, and (3) 40.0% using GP-LCB. The

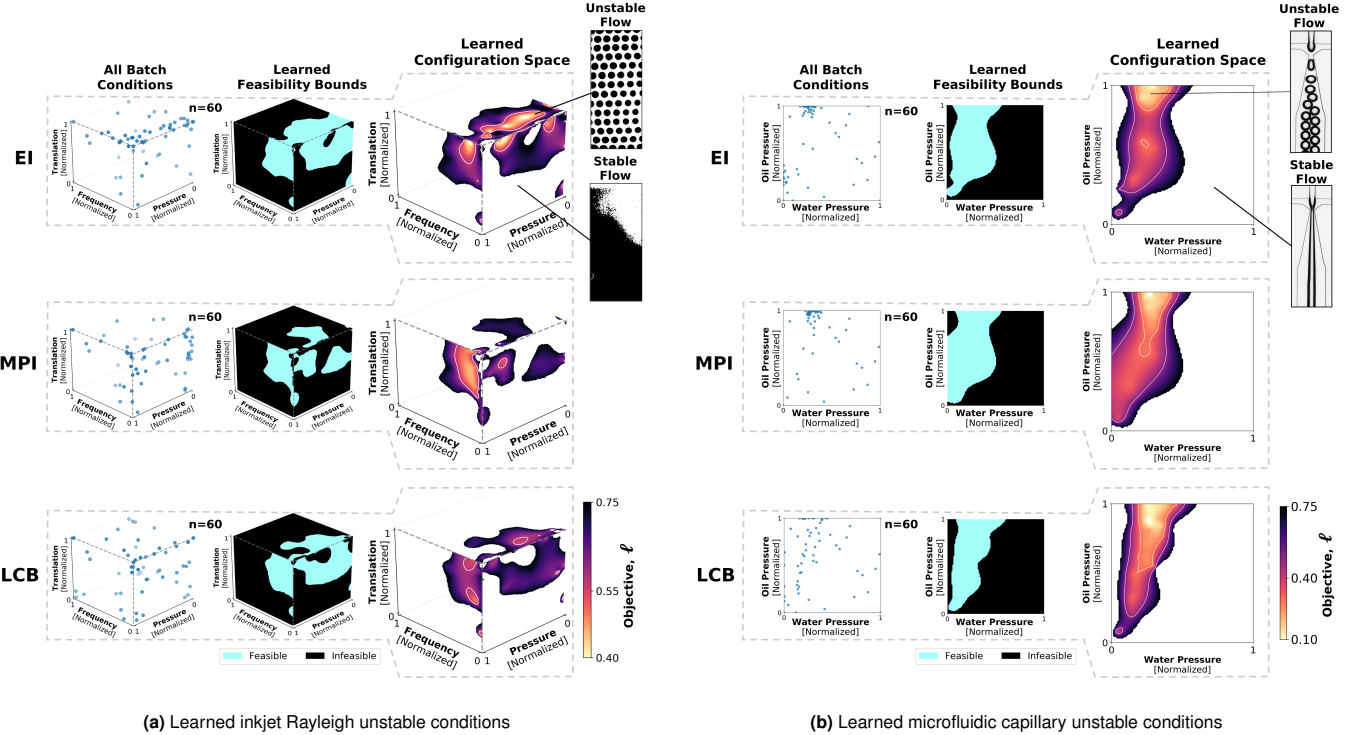


Fig. 5. Learned topology of the (a) inkjet and (b) microfluidic configuration spaces where fluid instability is feasible and droplets are optimized for uniformity and yield. The batch condition plots show where each of the Gaussian process (GP) acquisition functions, GP-Expected Improvement (EI), GP-Maximum Probability of Improvement (MPI), and GP-Lower Confidence Bound (LCB), sample from within the configuration space over all four experimental batches and initialization. The learned feasibility bounds highlight the regions in the configuration space where each acquisition function discovered printing conditions with $\ell < 0.75$, demarcating where fluid instability is feasible and generates discrete droplets. The learned configuration space topology quantifies the quality of samples within the feasibility bounds using ℓ . (a) The three acquisition functions consistently discover optimized droplet printing conditions for inkjet system in low piezoelectric frequency and high axial translation speed conditions, extending over the whole range of pressure. (b) The three acquisition functions consistently discover optimized droplet printing conditions for the microfluidic system in low-mid range water pressure and high oil pressure conditions.

Rayleigh feasibility bounds learned by each policy make up the following percentages of the total configuration space: (1) 34.2% using GP-EI, (2) 24.0% using GP-MPI, and (3) 28.7% using GP-LCB.

For the microfluidic system, the autonomous optimization loop repeatedly discovers the feasible conditions for capillary instability to be in low-mid range water pressure values for the whole range of oil pressure values using different decision policy acquisition functions, as shown in Fig. 5b. However, the most optimized unstable fluid conditions that generate uniform and high-yield droplets exist in mid range pressure, low frequency, and high translation conditions for the inkjet system and in mid range water pressure and high oil pressure conditions for the microfluidic system. Within four sequential iterations of acquired sample batches, the following percentages of samples lie within the capillary feasibility bounds for each policy: (1) 67.5% using GP-EI, (2) 97.5% using GP-MPI, and (3) 75.0% using GP-LCB. The capillary feasibility bounds learned by each policy make up the following percentages of the total configuration space: (1) 34.9% using GP-EI, (2) 38.0% using GP-MPI, and (3) 29.4% using GP-LCB.

4. Discussion

Our work addresses the challenge of a researcher optimizing a material system through pure experimentation without the aid and guidance of a domain expert. It is often the case where no analytical function exists to map hardware process conditions

to a target material property, thus, resulting in wasteful trial-and-error experimentation to discover the conditions which optimize that target property. We demonstrate the ability of an autonomous Bayesian optimization framework, integrated with a computer vision based objective, to discover hardware conditions that optimize a target material property using only 60 experimentally generated samples, without guidance from a domain expert.

We demonstrate that for these fluid printing systems that generate droplets at different length scales, an autonomous optimization loop learns where it is feasible to have unstable fluid printing conditions in a given N -dimensional configuration space through a computer vision-computed objective in lieu of a conventional domain expert. Using these results, a researcher can design a highly-optimized fluid system by engineering hardware that operates precisely within the printing condition ranges of minimum objective value. The full, unconstrained operable range of printing conditions define the dimensions of the configuration space for both fluid systems. The developed computer vision and machine learning algorithm is shown to have two-fold generalizability where the success of finding Plateau-Rayleigh unstable conditions from an unconstrained configuration space is demonstrated (1) at multiple length scales (millimeter and micrometer) and (2) for both 2- and 3-dimensional configuration spaces. The performance of this algorithm is illustrated using three independent experiments, each with a different acquisition function

but with the same initialization dataset: (1) GP-EI, (2) GP-MPI, and (3) GP-LCB. After four batches of sampling and model updates, all three experiments converge to comparable unstable fluid regions for both fluid systems; for the inkjet system, converged conditions are the full pressure range, low piezoelectric frequencies, and high axial translation speeds; for the microfluidic system, converged conditions are low-mid water pressures and high oil pressures. However, each of these acquisition functions has different sampling efficiencies where functions that learned to sample most points within the instability feasibility bounds performed better. The highest performing function for the inkjet system is GP-EI where 65.0% of sampled points are within the feasibility bounds and for the microfluidic system is GP-MPI where 97.5% of sampled points are within the feasibility bounds.

These results tell us that for a system of higher dimensionality with more complexity in its configuration space (the inkjet system), GP-EI, which scales the probability of improvement with the magnitude of improvement, is able to discover more optima conditions than GP-MPI or GP-LCB to contribute to efficient discovery of optimized droplet printing conditions. Conversely, for a system of lower dimensionality with less complexity in its configuration space (the microfluidic system), GP-MPI, which only acquires data based on the unscaled probability of improvement, has a higher optima discovery rate than GP-EI or GP-LCB.

The configuration space results reported in this paper illustrate the ability for algorithms to tune our experimental hardware in the place of a domain expert such that optimized products are consistently output. These results also provide useful insight for researchers to design novel, highly-optimized fluid systems since the ranges of each experimental condition that produce these optimized outputs are clearly reported. Through this robust method of experimentation demonstrated in our paper, different fluid systems are optimized autonomously without domain expert intervention to discover uniform and high-yield droplet conditions using only 60 samples. This method is evaluated using three different driving acquisition functions over three independent experiments, all which produce comparable optimization results.

ACKNOWLEDGMENTS. We thank James Serdy (MIT) for knowledge contributions and engineering expertise in hardware development and running physical experiments. We thank Dr. Armi Tiihonen for guidance and assistance with Bayesian optimization of physical systems. We thank Dr. Shijing Sun for contributions to methodology development and framing of this paper. This material is based upon work primarily supported by the Center to Center (C2C) International Collaboration on Advanced Photovoltaics as part of the Engineering Research Center Program of the National Science Foundation and the Office of Energy Efficiency and Renewable Energy of the Department of Energy under NSF Cooperative Agreement No. EEC-1041895. Iddo Drori would like to thank Google for a cloud research grant.

5. References

1. M Song, et al., Overcoming Rayleigh–Plateau instabilities: Stabilizing and destabilizing liquid–metal streams via electrochemical oxidation. *Proc. Natl. Acad. Sci.* **117**, 19026–19032 (2020).
2. DT Papageorgiou, On the breakup of viscous liquid threads. *Phys. Fluids* **7**, 1529–1544 (1995).
3. CC Mei, Lecture 5: Fluid jets in *Advanced Fluid Mechanics*. (Massachusetts Institute of Technology), (2004).
4. H Gu, MH Duits, F Mugele, Droplets formation and merging in two-phase flow microfluidics. *Int. J. molecular sciences* **12**, 2572–2597 (2011).
5. J Drugowitsch, AG Mendonça, ZF Mainen, A Pouget, Learning optimal decisions with confidence. *Proc. Natl. Acad. Sci.* **116**, 24872–24880 (2019).
6. P Hennig, CJ Schuler, Entropy search for information-efficient global optimization. *J. Mach. Learn. Res.* **13**, 1809–1837 (2012).
7. M Seeger, Gaussian processes for machine learning. *Int. journal neural systems* **14**, 69–106 (2004).
8. Wv Ohnesorge, The formation of drops by nozzles and the breakup of liquid jets (2019).
9. CN Baroud, F Gallaire, R Dangla, Dynamics of microfluidic droplets. *Lab on a Chip* **10**, 2032–2045 (2010).
10. AS Utada, A Fernandez-Nieves, HA Stone, DA Weitz, Dripping to jetting transitions in coflowing liquid streams. *Phys. review letters* **99**, 094502 (2007).
11. GH McKinley, M Renardy, Wolfgang von Ohnesorge. *Phys. Fluids* **23**, 127101 (2011).
12. C Clanet, JC Lasheras, Transition from dripping to jetting. *J. Fluid Mech.* **383**, 307–326 (1999).
13. J Tai, HY Gan, YN Liang, BK Lok, Control of Droplet Formation in Inkjet Printing Using Ohnesorge Number Category: Materials and Processes in 2008 10th Electronics Packaging Technology Conference. (IEEE), pp. 761–766 (2008).
14. D Bash, et al., Machine learning and high-throughput robust design of P3HT-CNT composite thin films for high electrical conductivity (2020).
15. S Langner, et al., Beyond Ternary OPV: High-Throughput Experimentation and Self-Driving Laboratories Optimize Multicomponent Systems. *Adv. Mater.* **32** (2020).
16. S Sun, et al., Accelerated Development of Perovskite-Inspired Materials via High-Throughput Synthesis and Machine-Learning Diagnosis. *Joule* **3**, 1437–1451 (2019).
17. S Sun, et al., A data fusion approach to optimize compositional stability of halide perovskites. *Matter* **4** (2021).
18. Z Ren, et al., Embedding physics domain knowledge into a Bayesian network enables layer-by-layer process innovation for photovoltaics. *npj Comput. Mater.* **6**, 1–9 (2020).
19. M Joanicot, A Ajdari, Droplet control for microfluidics. *Science* **309**, 887–888 (2005).
20. S Lignel, AV Salsac, A Drelich, E Leclerc, I Pezron, Water-in-oil droplet formation in a flow-focusing microsystem using pressure-and flow rate-driven pumps. *Colloids Surfaces A: Physicochem. Eng. Aspects* **531**, 164–172 (2017).
21. M Jeyhani, V Gnyawali, N Abbasi, DK Hwang, SS Tsai, Microneedle-assisted microfluidic flow focusing for versatile and high throughput water-in-water droplet generation. *J. colloid interface science* **553**, 382–389 (2019).
22. T Cubaud, TG Mason, Capillary threads and viscous droplets in square microchannels. *Phys. fluids* **20**, 053302 (2008).
23. SL Anna, HC Mayer, Microscale tipstreaming in a microfluidic flow focusing device. *Phys. Fluids* **18**, 121512 (2006).
24. IB Fridman, GS Ugolini, V VanDelinder, S Cohen, T Konry, High throughput microfluidic system with multiple oxygen levels for the study of hypoxia in tumor spheroids. *Biofabrication* **13**, 035037 (2021).
25. Y Ding, PD Howes, AJ deMello, Recent advances in droplet microfluidics. *Anal. chemistry* **92**, 132–149 (2019).
26. L Shang, Y Cheng, Y Zhao, Emerging droplet microfluidics. *Chem. reviews* **117**, 7964–8040 (2017).
27. G Kaufman, et al., Soft microcapsules with highly plastic shells formed by interfacial polyelectrolyte–nanoparticle complexation. *Soft Matter* **11**, 7478–7482 (2015).
28. MG Bah, HM Bilal, J Wang, Fabrication and application of complex microcapsules: A review. *Soft Matter* **16**, 570–590 (2020).
29. H Huang, et al., Generation and manipulation of hydrogel microcapsules by droplet-based microfluidics for mammalian cell culture. *Lab on a Chip* **17**, 1913–1932 (2017).
30. M Sesen, T Alan, A Neild, Droplet control technologies for microfluidic high throughput screening (μHTS). *Lab on a Chip* **17**, 2372–2394 (2017).
31. CP Barnes, D Silk, X Sheng, MPH Stump, Bayesian design of synthetic biological systems. *Proc. Natl. Acad. Sci.* **108**, 15190–15195 (2011).
32. MD McKay, RJ Beckman, WJ Conover, A comparison of three methods for selecting values of input variables in the analysis of output from a computer code. *Technometrics* **42**, 55–61 (2000).
33. E Brochu, VM Cora, N de Freitas, A Tutorial on Bayesian Optimization of Expensive Cost Functions, with Application to Active User Modeling and Hierarchical Reinforcement Learning (2010).
34. P Garstecki, HA Stone, GM Whitesides, Mechanism for flow-rate controlled breakup in confined geometries: A route to monodisperse emulsions. *Phys. review letters* **94**, 164501 (2005).

S1. Supporting Information

For each loop of optimization, the regions of the configuration space where new optima are acquired by each decision policy are highlighted in dark blue in Figure S1 for the inkjet system and in Figure S2 for the microfluidic system. For each of these sampled batches, all of the acquired points are plotted as box plots to illustrate the ranges of objective values. This information is useful when designing a fluid system such that a researcher may engineer the system to have experimental parameter values within the regions of high acquisition value.

Figure S3 illustrates the running minimum objective value across all sampled points for the inkjet and microfluidic systems. As the autonomous optimization procedure runs, more highly-optimized droplet structures are discovered.

The importance impact of each experimental parameter on the objective value ℓ is illustrated in Figure S4. For the inkjet system, frequency is illustrated to have a much larger impact on the objective value compared to pressure and translation speed. For the microfluidic system, water pressure is illustrated to have only a marginally larger impact on the objective value compared to the water pressure. These results are useful for designing new fluid systems since understanding the impact of a system's input on the output product provides insight into which input parameters should receive more attention during tuning.

An additional design condition is presented in Figure S5 for the microfluidic system, auxiliary to the design conditions presented in Figure 5. These design conditions illustrate the (a) objective value, (b) droplet diameter, and (c) number of droplets per row for the Capillary number (Ca) and Weber number (We) conditions of each printed droplet pattern. Tuning the system's properties to achieve desired droplet conditions are illustrated here as a function of Ca and We.

The configuration space envelope for each BO acquisition function shown in Figures 5 and S5 correlate to previous studies experimental results. Where a certain flow or linear pressure ratio. The slope of the linear ratio correlation will change for different microfluidics devices. The width of the instability drop formation region will change as a result of the fluids characteristics, such as viscosity ratio. Where in the upper section oil pressure is exceeding this ratio and, as a result leading to no water flow or water back-flow. In the lower section, the water pressure exceeding this ratio and forms an unbroken water stream. In addition, in the specific case of flow-focusing microsystem, the drop formation region can be divided into three distinguished sections. The first regime, "squeezing" or "geometric restriction", appears at the low flows/pressures and low capillary number area. The inner fluid is touching the restriction wall before breaking into individual drops (34). In the squeezing regime, there is a good correlation between the drop size and the fluid flow fraction. The second regime, "dripping" or "transition" appearing at the midrange flows/pressures and capillary number. In this regime, the formation of the droplets is due to the continuous liquid increase flow velocity inside the restrictions that leads to a pinched of droplets where the droplets fluid don't touch the constriction walls. In this case, smaller droplets can be formed, and as we are increasing the fraction ratio between the inner and continuous liquids, we can also receive a high volume of small drops. The third regime is the "jetting" that appears at the highest pressures and capillary numbers, where the droplets forming after the restriction.

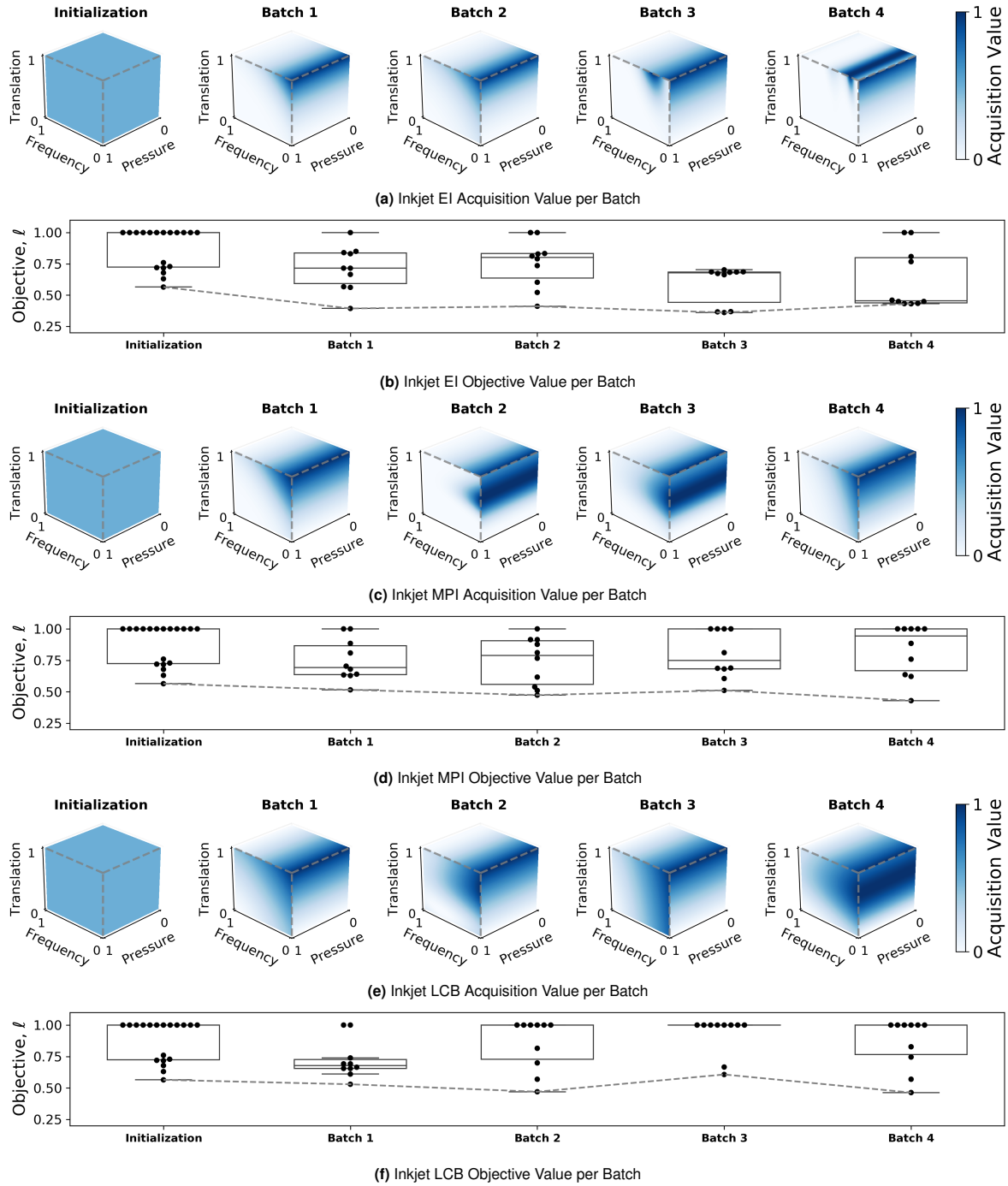


Fig. S1. Acquisition function search spaces by batch in 3-dimensions. The regions where each acquisition function is likely to draw points from within the inkjet configuration space are illustrated in blue – these denote regions of high acquisition value. The initialization acquisition space is a uniform color because points are picked uniformly during initialization via LHS. Based on the mechanics of each acquisition function, the acquisition value is computed by balancing the exploitation of the GP posterior mean and exploring the GP (co)variance. The acquisition search space evolves each loop which updates the sampling locations of data points (shown by the boxplots and Figure 3a). The reason why the same data point that maximizes the acquisition value is not sampled 10 times for every batch in the loop is because of evaluator used is local penalization – points sampled close to each other are penalized, thus, the best point is selected first, then the second best (within some distance), and so on.

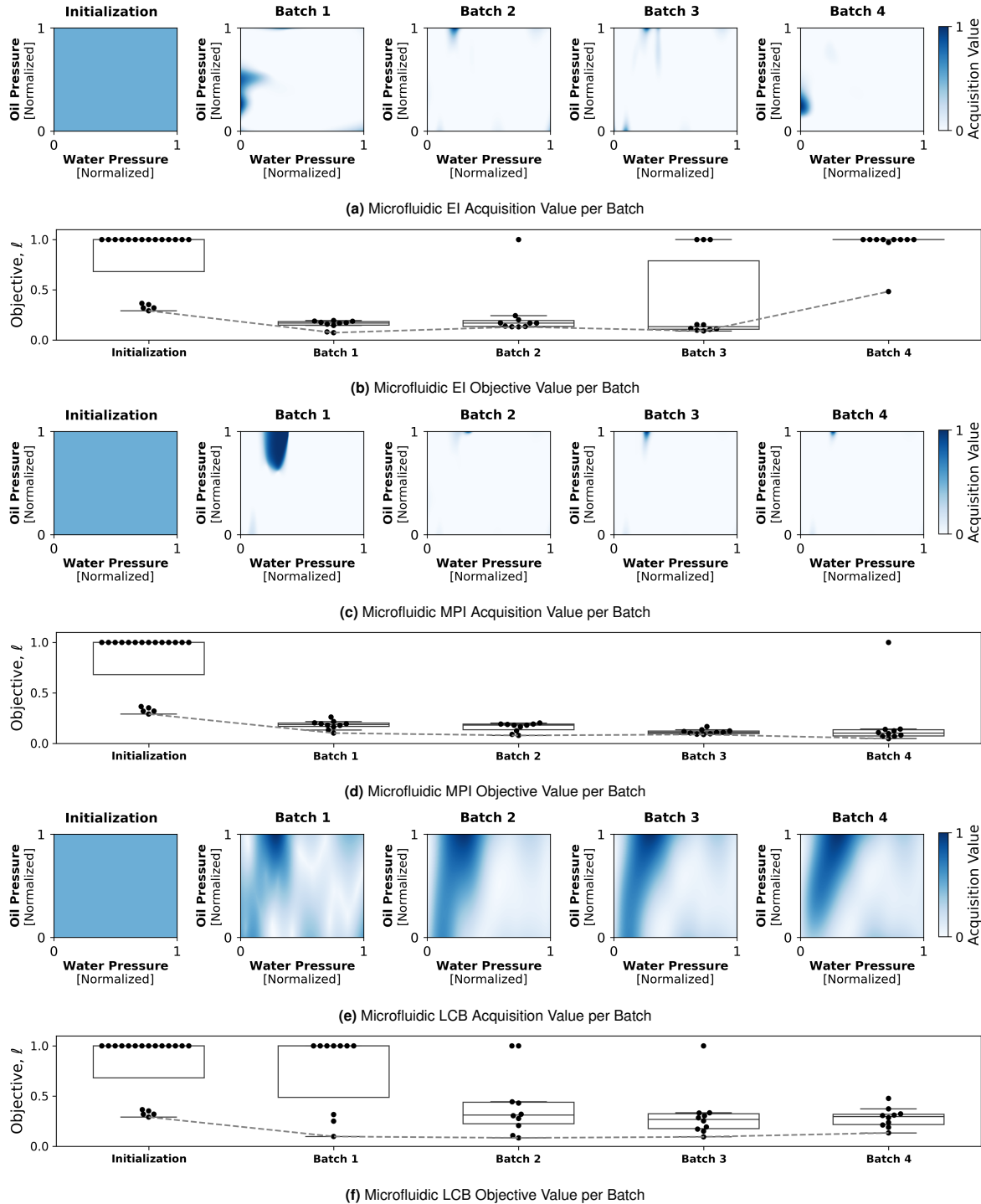


Fig. S2. Acquisition function search spaces by batch in 2-dimensions. The regions where each acquisition function is likely to draw points from within the microfluidic configuration space are illustrated in blue – these denote regions of high acquisition value. The initialization acquisition space is a uniform color because points are picked uniformly during initialization via LHS. Based on the mechanics of each acquisition function, the acquisition value is computed by balancing the exploitation of the GP posterior mean and exploring the GP (co)variance. The acquisition search space evolves each loop which updates the sampling locations of data points (shown by the boxplots and Figure 3b). The reason why the same data point that maximizes the acquisition value is not sampled 10 times for every batch in the loop is because of evaluator used is local penalization – points sampled close to each other are penalized, thus, the best point is selected first, then the second best (within some distance), and so on.

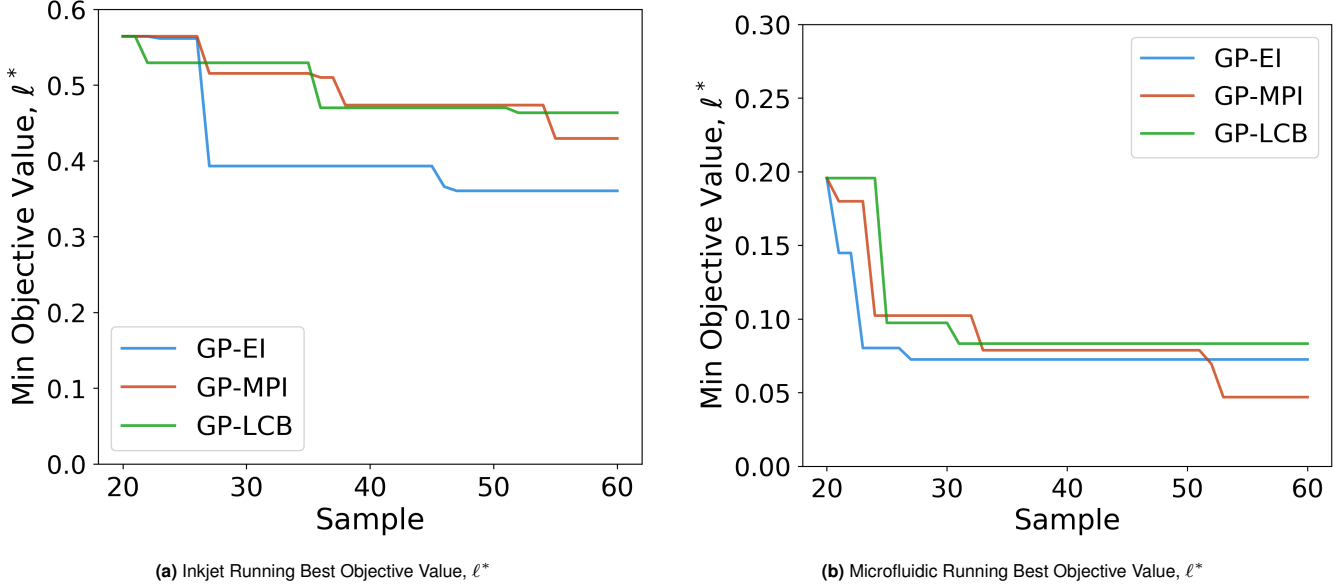


Fig. S3. The running minimum objective function evaluation ℓ^* for (a) the inkjet system and (b) the microfluidic system. The optimum unstable fluid conditions that generate high yield and high uniformity droplets are labeled by $\ell^* \in [0, 1]$ – the running minimum objective value. ℓ^* as a function of sample number is illustrated for each acquisition function after the 20 LHS initialization data points. The vertical axes are scaled differently for the inkjet and microfluidics systems, this scaling is arbitrary and is a result of the different droplet generating dynamics within each configuration space.

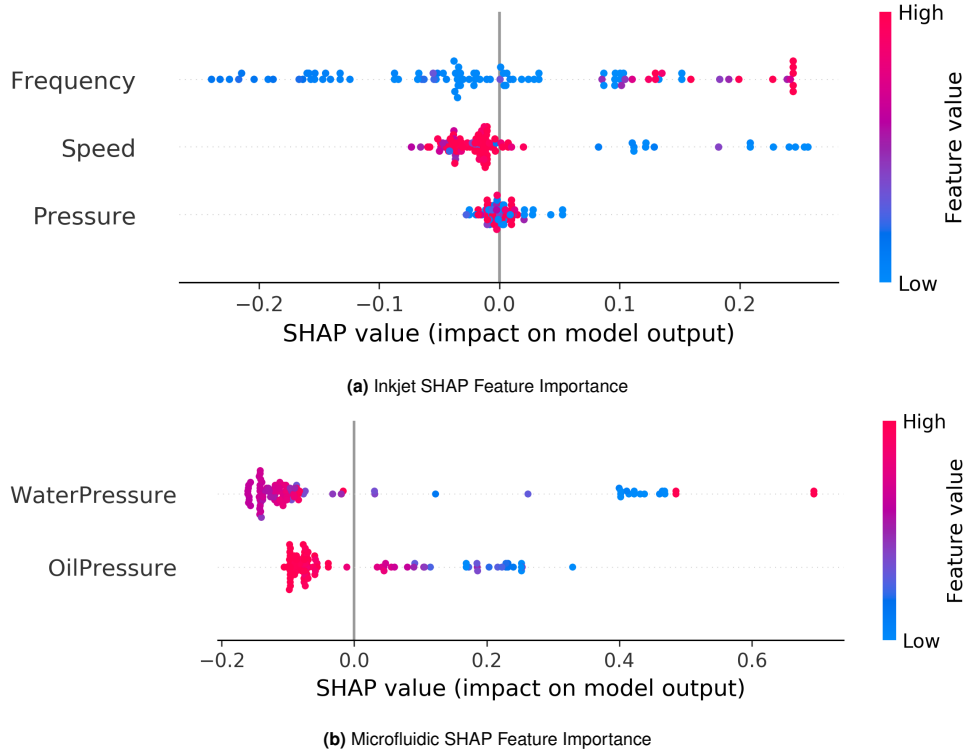


Fig. S4. The SHAP feature importance of the (a) inkjet and (b) microfluidic systems. Random forest regression with an 80/20 training/test split is used to compute the SHAP feature importance of all acquisition function-sampled data. Each printing condition is shown to have a certain SHAP value – the magnitude of the SHAP value describes how much that condition impacts the objective values ℓ . For example, low frequency values (blue) are shown to generate low ℓ values (high yield, uniform droplets), *i.e.*, illustrated by high negative SHAP values; high frequency values (red) are shown to generate high ℓ values (low yield, not uniform droplets), *i.e.*, illustrated by high positive SHAP values. High speed values have little impact on ℓ , whereas low speed values generate high ℓ values. Pressure, in general, has little impact on ℓ , shown by the clustering of all values of pressure conditions centered on a 0.0 SHAP value.

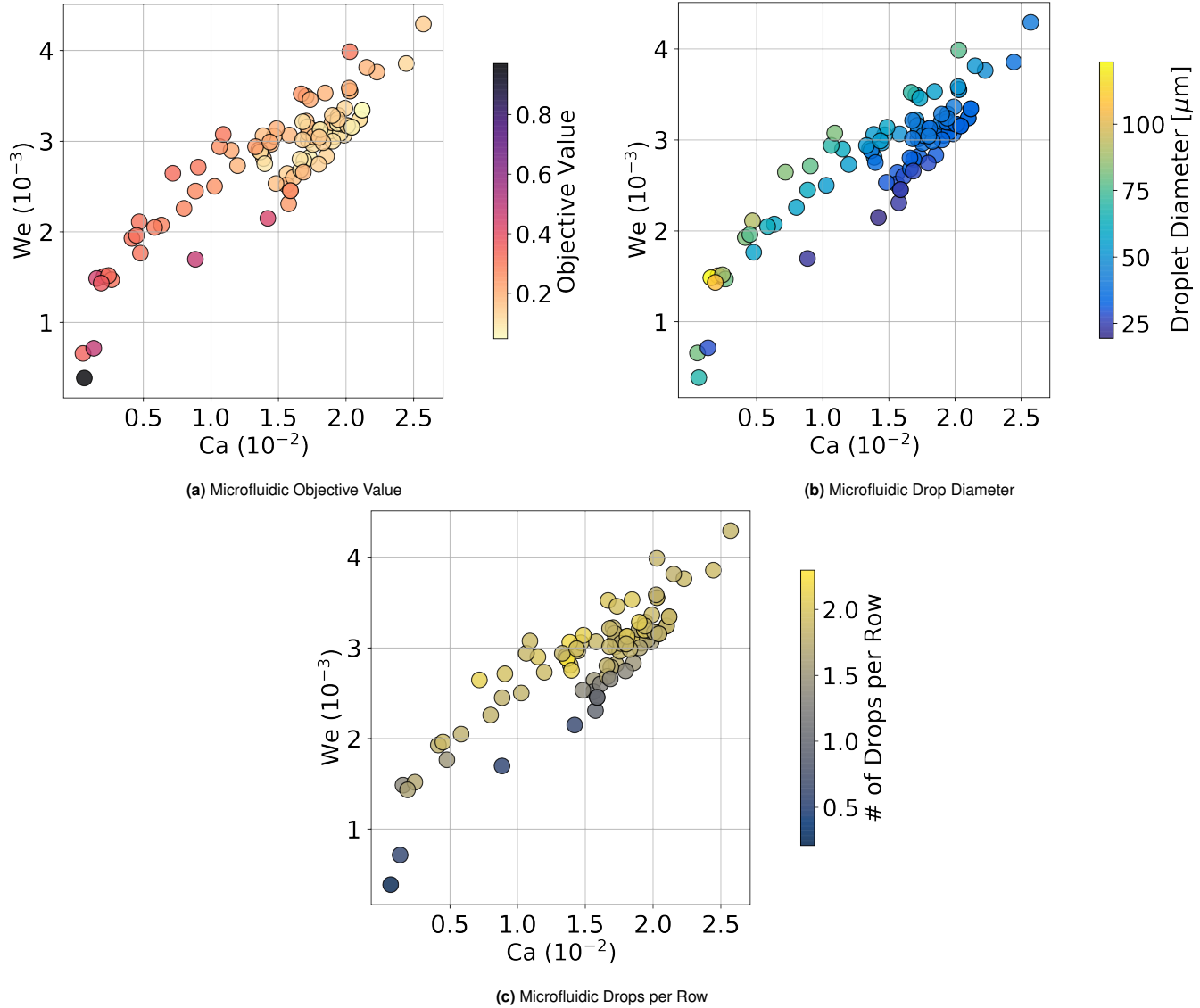


Fig. S5. Scatter diagram of (a) Objective Value ℓ , (b) Drop diameter, and (c) Average number of drops per row with respect to Weber and Capillary numbers within the microfluidic system. Where the velocity and fluid density are referring to the continues phase (mineral oil) and the interfacial tensions for water in oil.